Eur. Phys. J. Special Topics **225**, 2369–2387 (2016)

DOI: 10.1140/epjst/e2016-60060-2

THE EUROPEAN PHYSICAL JOURNAL SPECIAL TOPICS

Regular Article

Swimming in external fields

Holger Stark[a]

Institut für Theoretische Physik, Technische Universität Berlin, Hardenbergstr. 36, 10623 Berlin, Germany

Received 24 February 2016 / Received in final form 9 April 2016
Published online 10 November 2016

Abstract. Microswimmers move autonomously but are subject to external fields, which influence their swimming path and their collective dynamics. With three concrete examples we illustrate swimming in external fields and explain the methodology to treat it. First, an active Brownian particle shows a conventional sedimentation profile in a gravitational field but with increased sedimentation length and some polar order along the vertical. Bottom-heavy swimmers are able to invert the sedimentation profile.

Second, active Brownian particles interacting by hydrodynamic flow fields in a three-dimensional harmonic trap can spontaneously break the isotropic symmetry. They develop polar order, which one can describe by mean-field theory reminiscent to Weiss theory of ferromagnetism, and thereby pump fluid.

Third, a single microswimmer shows interesting non-linear dynamics in Poiseuille flow including swinging and tumbling trajectories. For pushers, hydrodynamic interactions with bounding surfaces stabilize either straight swimming against the flow or tumbling close to the channel wall, while pushers always move on a swinging trajectory with a specific amplitude as limit cycle.

1 Introduction

Understanding the non-equilibrium behavior of microswimmers is one of the major challenges at the interface of physics, biology, and also chemical engineering [1–3]. Their emergent collective dynamics is a most fascinating topic. Interacting microswimmers may show turbulence at low Reynolds number [4] and exhibit dynamic clustering due to phoretic interactions [5–7] or motility-induced phase separation [8–13]. Their collective motion drives macroscopic fluid flow as in bioconvection [15] or vortex formation [16]. Hydrodynamic interactions between microswimmers crucially determine their collective patterns [17–24].

With external fields one is able to control microswimmers and induce novel phenomena even on the single particle level. Under gravity active particles show conventional sedimentation [25] but also develop polar order [26]. Microswimmers can invert the sedimentation profile, when they are bottom-heavy [27], which then initiates bioconvection [15] or the formation of phytoplankton layers in the coastal ocean [28].

[a] e-mail: holger.stark@tu-berlin.de

In a harmonic trap potential, hydrodynamically interacting microswimmers undergo spontaneous symmetry breaking and develop a fluid pump [29,30].

Microswimmers react on shear flow and either decrease or increase the effective fluid viscosity depending on their mean orientation and their swimmer type as pullers or pushers [31]. Both cases have been observed in experiments together with shear thinning [32,33] and superfluid behavior, where the effective shear viscosity becomes zero [34,35]. External fluid flow can lead to aggregation [36] and trapping [37]. Under Poiseuille flow microswimmers exhibit interesting nonlinear swimming dynamics [38,39] and they develop non-uniform density profiles [40].

In the following, we review the rich phenomenology of swimming in external fields through examples from our own studies. We deal with active particles under gravity in Sect. 2.1 and in a harmonic trap potential in Sect. 2.2. Finally, we consider the ideal situation of a microswimmer under Poiseuille flow in Sect. 3.

2 Active Brownian particles in external potentials

Before we discuss two examples, how active Brownian particles behave in external potentials, we summarize a few of their properties. Passive spherical colloids with radius a perform translational and rotational Brownian motion in a Newtonian fluid with viscosity η. The respective diffusion coefficients obey the Stokes-Einstein relations

$$D = \frac{k_B T}{\gamma} = \frac{k_B T}{6\pi\eta a} \quad \text{and} \quad D_r = \tau_r^{-1} = \frac{k_B T}{\gamma_r} = \frac{k_B T}{8\pi\eta a^3}, \tag{1}$$

where $\gamma = 6\pi\eta a$ and $\gamma_r = 8\pi\eta a^3$ are the respective Stokes friction coefficients for translation and rotation. The temporal correlations of a fixed direction within the colloid, described by the unit vector $\boldsymbol{e}$, decay by rotational diffusion within the decorrelation time $\tau_r = D_r^{-1}$. Hence $\langle \boldsymbol{e}(0) \cdot \boldsymbol{e}(t) \rangle = \exp(-2D_r t)$, where $\boldsymbol{e}(t)$ refers to the dynamics of the orientation as seen in the laboratory frame.

In a next step we make the colloids active so that they move with a velocity v_0 along the intrinsic particle direction $\boldsymbol{e}(t)$. To compare active motion to thermal translational diffusion, we consider the ratio of times the particle needs to diffuse a particle radius a (time $t_d = a^2/D$) and to move ballistically along a (time $t_b = a/v_0$). This gives the Péclet number $\mathrm{Pe} = t_d/t_b = v_0 a/D$, where large Pe means activity dominates. For times smaller than the decorrelation time τ_r, the active colloid performs ballistic motion along a distance $v_0\tau_r$. To compare it to the particle radius, we introduce the persistence number $\mathrm{Pe}_r = v_0\tau_r/a$ and $\mathrm{Pe}_r \gg 1$ then means persistent motion in one direction. Since the orientation of the active colloid decorrelates with time, the colloid crosses over to diffusive motion beyond τ_r with an effective diffusion coefficient [42]

$$D_{\mathrm{eff}} = D + v_0^2/(6D_r) = D(1 + 2\mathrm{Pe}^2/9)\,. \tag{2}$$

For the second equality, we have used Eqs. (1) and $\mathrm{Pe} = v_0 a/D$. With this summary of basic features of active Brownian particles, we now turn towards two examples illustrating new properties, which arise when active particles move in external potentials.

2.1 A dilute active suspension under gravity

2.1.1 Sedimentation and polar order

The first example is motivated by experimental work of the Lyon group on the sedimentation of a dilute suspension of active particles under gravity [25]. Their main

result was that active particles like passive colloids exhibit an exponential sedimentation profile in density. However, the sedimentation length increases with the activity of the colloids. To explain the basic phenomenology, we introduce the total probability density $\Omega(z)$ to find an active colloid at height z under gravity. The exponential sedimentation profile develops since the diffusional and gravitational drift current balance each other,

$$(-D_{\text{eff}}\nabla_z - mg/\gamma)\Omega(z) = 0, \tag{3}$$

where $-mg/\gamma$ is the sedimentation velocity with m the colloidal mass and g the gravitational acceleration. Note that the diffusional current is written with the effective diffusion constant. The balance equation is solved by an exponential profile with an effective sedimentation length:

$$\Omega(z)/\Omega(0) = \exp(-z/\delta_{\text{eff}}) \quad \text{with} \quad \delta_{\text{eff}} = (1 + 2\text{Pe}^2/9)\delta_0\,. \tag{4}$$

Here, $\delta_0 = k_BT/mg$ is the sedimentation length of passive colloids, where thermal energy k_BT and potential energy $mg\delta_0$ are just equal. Due to activity one finds that δ_{eff} grows proportional to $\text{Pe}^2 \propto v_0^2$ as observed in the experiments. The second term arises from the active part of D_{eff}.

Why does the sedimentation length increase with the activity of the colloids? The reason is that the colloids develop a polar order along the vertical with the colloids biased to swim upwards [26]. Such a polar order develops since an isotropic distribution of the colloidal orientation $\boldsymbol{e}$ is unstable. To see this, we consider a local volume in an exponential density profile. More particles swimming upwards enter this volume from below than leaving it upwards. Equally, less particles swimming downwards enter the volume from above than leaving it downwards. So, polar order of upwards swimming particles has to develop in the volume and hence in the sedimentation profile. In principle, this scenario steadily increases the local polar order. However, the non-uniform orientational distribution also generates a rotational diffusive current (see below), which always rotates upwards into downwards swimming active colloids. Thus the polar order becomes stationary.

We now formulate this idea more rigorously using the Smoluchowsky equation for the probability distribution function $\rho(\boldsymbol{r}, \boldsymbol{e}, t)$, which includes the colloidal orientation and is normalized to one [26,27]. We write the Smoluchowski equation as a continuity equation for probability,

$$\frac{\partial \rho}{\partial t} + \nabla \cdot \boldsymbol{J}^{\text{trans}} + \mathcal{R} \cdot \boldsymbol{J}^{\text{rot}} = 0, \tag{5}$$

with the respective translational and rotational currents

$$\boldsymbol{J}^{\text{trans}} = -D\nabla\rho + (v_0\boldsymbol{e} + m\boldsymbol{g}/\gamma)\,\rho \quad \text{and} \quad \boldsymbol{J}^{\text{rot}} = -D_r\mathcal{R}\rho\,. \tag{6}$$

Here, $\boldsymbol{J}^{\text{trans}}$ contains contributions from thermal diffusion and active and gravitational drift motion. The rotational current is purely diffusive with the rotational operator $\mathcal{R} = \boldsymbol{e} \times \nabla_{\boldsymbol{e}}$.

To treat Eq. (5), we deviate from our original approach in Ref. [26] and use the formalism of a multipole expansion in the orientation vector $\boldsymbol{e}$ as outlined in Refs. [7,27,43]. We formulate the multipole expansion for the full distribution function:

$$\rho(\boldsymbol{r}, \boldsymbol{e}, t) = \frac{1}{4\pi}\left[\Omega(\boldsymbol{r}, t) + 3\boldsymbol{P}(\boldsymbol{r}, t)\cdot\boldsymbol{e} + \frac{15}{2}\boldsymbol{Q}(\boldsymbol{r}, t)\cdot(\boldsymbol{e}\otimes\boldsymbol{e} - \frac{1}{3}\mathbf{1}) + \ldots\right], \tag{7}$$

where we introduce the total probability density $\Omega(\boldsymbol{r}, t) = \int \rho(\boldsymbol{r}, \boldsymbol{e}, t)d^2e$ from above and the respective densities for the dipole and quadrupole moment,

$$\boldsymbol{P}(\boldsymbol{r}, t) = \int \boldsymbol{e}\rho(\boldsymbol{r}, \boldsymbol{e}, t)d^2e, \qquad \boldsymbol{Q}(\boldsymbol{r}, t) = \int (\boldsymbol{e}\otimes\boldsymbol{e} - \frac{1}{3}\mathbf{1})\rho(\boldsymbol{r}, \boldsymbol{e}, t)d^2e. \tag{8}$$

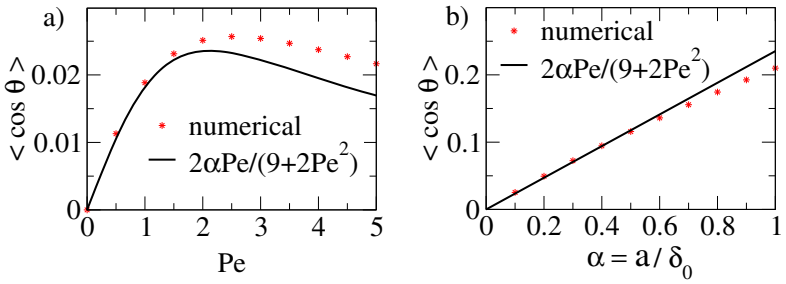

Fig. 1. Mean orientation along the vertical, $\langle \cos\theta \rangle$, plotted versus (a) $\mathrm{Pe} = v_0 a/D$ at $a/\delta_0 = 0.1$ and (b) $\alpha = a/\delta_0$ at $\mathrm{Pe} = 2$. Numerical data are computed from the steady solution of Eq. (6). [Reprinted with permission from Ref. [26]; Copyright (2011) by the American Physical Society.]

Note that $\boldsymbol{Q}$ is a second-rank tensor and the symbol "$\cdot$" in Eq. (7) means contraction over all indices. To derive a hierarchy of dynamic equations for the multipole moments, one multiplies Eq. (5) with one, $\boldsymbol{e}$, etc. and integrates over all orientations of $\boldsymbol{e}$. This gives dynamic equations for the total density and the polarization,

$$\partial_t \Omega + \nabla \cdot (-D\nabla + m\boldsymbol{g}/\gamma)\Omega + v_0 \nabla \cdot \boldsymbol{P} = 0 \tag{9}$$

$$\partial_t \boldsymbol{P} + \nabla \cdot (-D\nabla + m\boldsymbol{g}/\gamma)\boldsymbol{P} + 2D_r \boldsymbol{P} + v_0 \nabla \cdot \boldsymbol{Q} + (v_0/3)\nabla\Omega = 0\,. \tag{10}$$

In both equations, the leading moment couples to a higher moment through the active drift term. So, we need to close the hierarchy of equations. The polarization in Eq. (10) relaxes with the rate D_r, whereas the total density Ω is a hydrodynamic mode. Therefore, on time scales larger than $t_r = D_r^{-1}$, we can neglect the time derivative $\partial_t \boldsymbol{P}$ in Eq. (10). Second, we assume only a small contribution from $\boldsymbol{Q}$ and neglect it in the following. Finally, the moments ρ and $\boldsymbol{P}$ vary smoothly in space. Hence, in Eq. (10) we concentrate on the lowest or leading spatial gradients in both moments and thus arrive at $\boldsymbol{P} \approx -v_0/(6D_r)\nabla\Omega$. Inserted into Eq. (9), one obtains an additional diffusion term and thereby reproduces the effective diffusion constant of Eq. (2). Finally, with $\boldsymbol{g} = -g\boldsymbol{e}_z$ the translational current of the resulting Smoluchowski equation for Ω agrees with Eq. (3), and the sedimentation profile of Eq. (4) is recovered.

From the polarization $\boldsymbol{P}$ we can extract the mean orientation $\langle \cos\theta \rangle$ along the vertical where $\cos\theta = \boldsymbol{e}_z \cdot \boldsymbol{e}$. We introduce $P = \langle \cos\theta \rangle \Omega \approx -v_0/(6D_r)\nabla_z \Omega$ and ultimately arrive at

$$\langle \cos\theta \rangle \approx -\frac{2}{9} a\mathrm{Pe}\nabla_z \ln\Omega = \frac{2}{9}\frac{a}{\delta_0}\frac{\mathrm{Pe}}{1 + 2\mathrm{Pe}^2/9}\,, \tag{11}$$

where we used the exponential profile from Eq. (4), $\mathrm{Pe} = v_0 a/D$, and $D/D_r = 4a^2/3$.

Figure 1 compares numerical solutions of Eq. (5) with the approximate expression (11) for the mean orientation of the active colloids along the vertical. The range of Pe and $\alpha = a/\delta_0 = 0.1$ correspond to values used in the experiments of Ref. [25]. In graph (a) the analytic maximum at $\mathrm{Pe} = 3/\sqrt{2}$ is nearly reproduced by the numerical results, but clear deviations exist for $\mathrm{Pe} > 2$. Notably, for the experimental parameter $\alpha \sim 0.1$ the mean orientation $\langle \cos\theta \rangle$ is very small. In graph (b) we show the predicted linear dependence of $\langle \cos\theta \rangle$ on α. Since $\alpha \sim a^4$, the mean orientation is very sensitive to the particle radius and taking colloids with $a = 1\mu$m instead of 0.5μm (used in [25]) increases the mean orientation of particles from 2.5% to 20%. So, the anisotropy in the particle orientation should directly be observable. Note that α is also increased

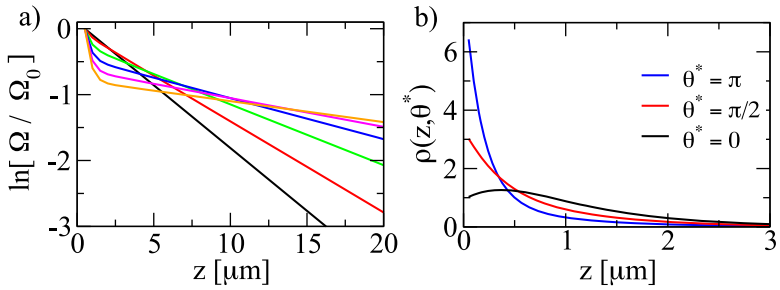

Fig. 2. (a) Logarithmic plot of the total density profile $\Omega(z)$ at $\alpha = a/\delta_0 = 0.1$. From the black to orange line, Pe increases from Pe = 0 to 5. (b) Altitude dependence of $\rho(z, \theta^*)$ for different orientation angles θ^* with the vertical. Other parameter values are $\alpha = 1$ and Pe = 2. [Reprinted with permission from Ref. [26]; Copyright (2011) by the American Physical Society.]

by tuning the gravitational acceleration g in a centrifuge. Our numerical solutions show, both the mean orientation $\langle \cos\theta \rangle$ and the sedimentation length δ_{eff} saturate when $\alpha = a/\delta_0$ increases beyond one and a perfectly ordered state occurs for $\alpha \to \infty$. However, for $\alpha > 1$ or $a > \delta_0$ passive particles accumulate at the bottom. So, active particles need a sufficiently large swimming velocity v_0 to create a density profile that extends to heights larger than the particle radius.

At bounding walls the sum of diffusive, active, and gravitational currents has to vanish for each orientation, so the boundary condition reads: $J_z^{\text{trans}} = 0 = -D\nabla_z\rho + (v_0 \cos\theta - mg/\gamma)\rho$. To determine a numerical solution of the Smoluchowski equation (5), we implemented the boundary condition at the bottom wall at $z = 0$ and at an upper wall. The numerically determined total density profile $\Omega(z)$ plotted in Fig. 2(a) clearly shows the exponential decay with height z and also the increase of the sedimentation length δ_{eff} with Pe. However, close to the bottom wall at $z = 0$ we observe a pronounced deviation from the bulk solution and a strong colloidal accumulation. The reason is that particles swim against the wall and stay there for some time. This leads to the observed accumulation with a strong polar order towards the wall, which is visible for the orientation angle $\theta^* = \pi$ in Fig. 2(b). In addition, particles swimming away from the wall ($\theta = 0$) are depleted. The authors of Ref. [25] also mention the wall accumulation in their experimental profiles but attribute it to some colloidal adsorption. However, our theory shows that this accumulation is solely due to the particle's active motion.

2.1.2 Influence of an aligning torque

We recently extended our investigations in Ref. [27] by considering bottom-heavy microswimmers [see inset of Fig. 3(a)]. When the center of mass of a spherical particle does not coincide with its geometrical center, a torque $\boldsymbol{M} = mr_0\boldsymbol{g} \times \boldsymbol{e} = mr_0 g\,\mathcal{R}\cos\theta$ aligns the intrinsic particle direction $\boldsymbol{e}$ along $-\boldsymbol{g}$.[1] We quantify the strengh of the aligning torque by refering the off-center distance to the sedimentation length, $r_0/\delta_0 = mr_0 g/(k_B T)$. In the Volvox algae a strong aligning torque, $r_0/\delta_0 \gg 1$, exists and hydrodynamic coupling between two algae leads to intricate bound states [44]. In particular, strong spinning around a body-fixed axis contributes substantially to

[1] While the gravitational force $m\boldsymbol{g}$ requires the buoyancy mass, the gravitational torque depends on the pure mass. Here we use the same symbol for them and account for a difference by redefining r_0.

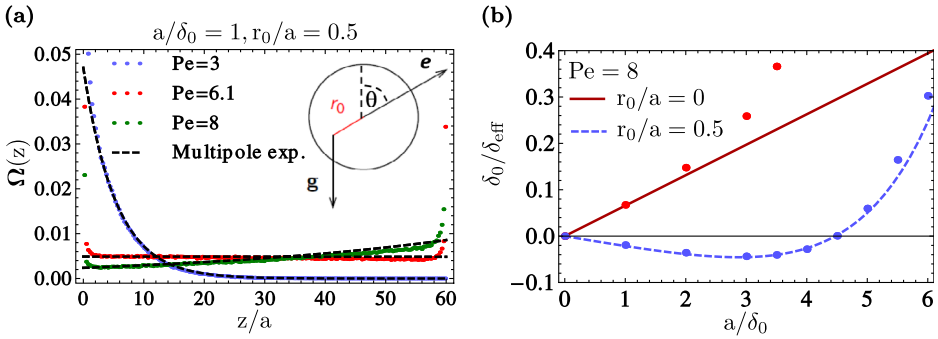

Fig. 3. (a) Spatial density profile $\Omega(z)$ for different Péclet numbers. Numerical data (dots) are computed from Brownian dynamics simulations, dashed lines belong to the analytic result from the multipole expansion. Inset: Bottom-heavy active particle with off-center distance r_0 between the geometrical and the center of mass. The particle moves in the gravitational field $\boldsymbol{g}$ along swimming direction $\boldsymbol{e}$. (b) Inverse sedimentation length $\delta_0/\delta_{\text{eff}}$ plotted versus gravitational strength a/δ_0 for non-bottom-heavy particles ($r_0 = 0$, red) and bottom-heavy particles ($r_0 = 0.5$, blue). Lines are theoretical predictions, dots are simulation results. [Adapted from Ref. [27] with kind permission of The European Physical Journal (EPJ).]

this hydrodynamic coupling [44]. It should be possible to make active Janus colloids bottom-heavy or use superparamagnetic colloids [45] or magnetic Janus spheres [46] to tune alignment by an external magnetic field. Finally, biological swimmers experience chemotaxis or phototaxis, where the respective aligning fields are the gradients of a chemical substance or the intensity of light [47].

To treat bottom-heaviness, we add an additional rotational current to the Smoluchowski Eq. (5) initiated by the aligning torque, $\boldsymbol{J}_A^{\text{rot}} = \boldsymbol{M}/\gamma_r\rho$. We have already introduced the rotational friction coefficient γ_r in Eqs. (1). Again, we derive a hierarchy of dynamic equations for the multipoles of $\rho(\boldsymbol{r}, \boldsymbol{e}, t)$, which now has to be closed on the level of the quadrupole density to observe the influence of the aligning torque [27]. Ultimately, we are able to derive a Smoluchowski equation for the total density $\Omega(\boldsymbol{r}, t)$, $\partial_t\Omega + \nabla \cdot (-D_{\text{eff}}\nabla + m\boldsymbol{g}_{\text{eff}}/\gamma)\Omega = 0$, where the aligning torque contributes to both the effective diffusion constant and an effective gravitational acceleration,

$$D_{\text{eff}} = D\left\{1 + \frac{2\text{Pe}}{9}\, c\left(\frac{r_0}{\delta_0}\right)\left[1 - \frac{1}{\text{Pe}}\frac{a r_0}{\delta_0^2}\, c\left(\frac{r_0}{\delta_0}\right)\right]\right\} \quad \text{and} \quad g_{\text{eff}} = g\left[1 - \frac{\text{Pe}}{3}\frac{r_0}{a}\, c\left(\frac{r_0}{\delta_0}\right)\right] \tag{12}$$

with $c(r_0/\delta_0) = [1 + (r_0/\delta_0)^2/15]^{-1}$. In the limit $r_0 = 0$, one obtains D_{eff} from Eq. (2) and $g_{\text{eff}} = g$. Interestingly, g_{eff} becomes negative for sufficiently large Pe. So, the torque aligning the active particles to swim preferentially upwards acts like a negative gravitational strength.

As before, we obtain an exponential sedimentation profile for the total density $\Omega(z, t)$, with sedimentation length $\delta_{\text{eff}} = \gamma D_{\text{eff}}/(m g_{\text{eff}})$. Profiles for different Péclet number Pe are plotted in Fig. 3(a) at fixed gravitational strength a/δ_0 and off-center distance r_0/a. Analytic predictions from the multipole expansion are compared with Brownian dynamics simulations. At a specific Péclet number Pe we observe an inversion of the sedimention profile, where the active colloids gather at the upper wall. This inversion takes place when g_{eff} in Eqs. (12) switches sign and becomes negative.

When the swimming speed cancels sedimentation, the density profile becomes uniform. The full distribution function simply becomes the Boltzmann distribution of a

particle orienting under the aligning torque, $\rho(z, \boldsymbol{e}) \propto \exp(r_0 \cos\theta/\delta_0)$, also known as Mises-Fisher distribution. Since the bounding walls enforce that the average translational drift current along the z direction is zero, one has $0 = v_0\langle\cos\theta\rangle - mg/\gamma$. Calculating $\langle\cos\theta\rangle$ from the Boltzmann distribution, we obtain

$$\mathrm{Pe}^* = \frac{a/\delta_0}{\coth(r_0/\delta_0) - \delta_0/r_0} \approx \frac{3a}{r_0} + \frac{ar_0}{5\delta_0^2} \tag{13}$$

for the activity Pe^*, where a uniform density profile occurs. The second approximate expression comes from the Laurent series and agrees with setting $g_{\mathrm{eff}} = 0$ in the right formula of Eqs. (12). Clearly, for $\delta_0 \to 0$ an infinite activity, $\mathrm{Pe}^* \to \infty$, is necessary to achieve a uniform density.

The sedimentation length $\delta_{\mathrm{eff}} = \gamma D_{\mathrm{eff}}/(mg_{\mathrm{eff}})$ calculated with the approximate expressions from Eqs. (12) becomes $\delta_{\mathrm{eff}} = -\delta_0\, 2a/(3r_0)$ in the limit $\mathrm{Pe} \to \infty$. We have checked its negative value also in our simulations. So a sufficiently strong particle activity always inverts the sedimentation profile. On the other hand, strong gravity ($\delta_0/a \to 0$), as realized in a centrifuge, completely determines the sedimentation profile and one obtains $\delta_{\mathrm{eff}} = \delta_0$. Figure 3(b) shows a negative inverse sedimentation length $\delta_{\mathrm{eff}}^{-1}$ for small gravitational strength a/δ_0, which becomes positive for increasing a/δ_0 (blue line). Without any aligning torque ($r_0 = 0$) δ_{eff} is always positive (red line). So, appropriately tuning a/δ_0 with a centrifuge makes it possible to separate bottom-heavy from non-bottom-heavy colloids. The mean alignment $\langle\cos\theta\rangle$ is calculated as before by determining the polarization $\boldsymbol{P}$ from the multipole expansion [27]. Qualitatively, we obtain similar graphs for varying Pe and a/δ_0 as in Fig. 1.

The inverted sedimentation profile becomes unstable under density fluctuations of interacting microswimmers at sufficiently large densities. This gives rise to pattern formation by bioconvection [48–50], albeit in a parameter regime of large Péclet numbers where thermal diffusion is small compared to active motion. The instability is also induced by hydrodynamic interactions between individual swimmers, as we have demonstrated in first simulations [51]. Artificial microswimmers offer the possibility of tuning their properties such as the swimming velocity and bottom-heaviness in the full parameter range. This will certainly reveal new emergent collective behavior, which we plan to investigate with full hydrodynamic simulations using appropriate microswimmer models.

2.2 Self-induced polar order in a three-dimensional harmonic trap

In the second example, dealing with microswimmers in an external potential, we address a specific situation, where hydrodynamic interactions between microswimmers induce emergent collective motion [30]. As before, we consider active Brownian particles with radius a, swimming velocity v_0, and orientation vector $\boldsymbol{e}_i$, which we place into a harmonic trap with radial trapping force $\boldsymbol{F}_i = -k_{\mathrm{trap}}\boldsymbol{r}_i$ realized, for example, by an optical tweezer. Here, the position vector $\boldsymbol{r}_i$ points from the center of the trap to particle i. In addition, we implement an effective hard-core repulsion between the active particles and, most importantly, hydrodynamic interactions [30].

This setup was studied before by Nash et al. for run-and-tumble particles using Lattice-Boltzmann simulations [29]. They observed the formation of a fluid pump, where all swimmers concentrate close to the center and align along each other, as illustrated in Fig. 4 (left). Thus the rotational symmetry of the harmonic trap is spontaneously broken. Since each of the swimmers pushes fluid backwards, a macroscopic fluid flow is initiated as also shown by Fig. 4 (left).

We performed Brownian dynamics simulations of N hydrodynamically interacting active particles. Details are given in Ref. [30]. The most important element is that each

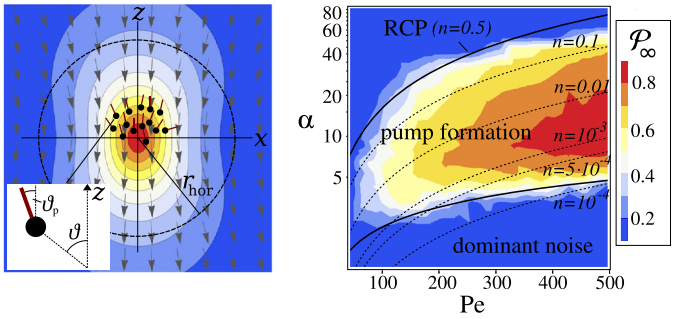

Fig. 4. (Left) Sketch of the fluid pump. Active particles concentrate in the upper half sphere and align along the z axis. The resulting flow field is illustrated by a regularized stokeslet. The dashed black circle with radius r_{hor} is the particles' horizon. (Right) The state diagram of pump formation in reduced trapping strength α versus Péclet number Pe shows the color-coded polar order parameter $\mathcal{P}_\infty$. Along the dashed lines density n is constant. At very high densities the active particles become randomly close packed (RCP) and cannot form a pump (upper solid curve). [Reprinted with permission from Ref. [30]; Copyright (2014) by the American Physical Society.]

trapping force acting on particle i initiates a Stokeslet flow field in the surrounding fluid,

$$\boldsymbol{u}(\boldsymbol{r}) = \frac{1}{8\pi r}\left[\mathbf{1} + \frac{(\boldsymbol{r}-\boldsymbol{r}_i)\otimes(\boldsymbol{r}-\boldsymbol{r}_i)}{|\boldsymbol{r}-\boldsymbol{r}_i|^2}\right]\boldsymbol{F}_i, \tag{14}$$

which translates and rotates neighboring particles. Without the Stokeslet and for sufficiently large Pe, the active particles collect at the horizon radius $r_{\mathrm{hor}} = \gamma v_0/k_{\mathrm{trap}}$, where they point radially outward. With hydrodynamic interactions included this situation becomes unstable and the fluid pump starts to form at sufficiently large Pe. The main effect is that the vorticity ω_{HI} of the flow field rotates the particles' orientations away from the radial direction. They move towards each other and generate denser regions, which become unstable. Deterministic rotation by fluid vorticity is counteracted by rotational diffusion and we expect the instability to set in when both rotational rates are similar, $\omega_{\mathrm{HI}} \sim D_r$. This amounts to a criterion for pump formation relating reduced trapping strength $\alpha = k_{\mathrm{trap}}a^2/(k_BT)$ to Péclet number and particle number, $\alpha \sim \sqrt{\mathrm{Pe}/N}$ [30].

Using the polar order parameter $\mathcal{P}_\infty = \left|\sum_{i=1}^{N} \boldsymbol{e}_i(t)\right|/N$, we measure the alignment of the active particles. Figure 4 (right) shows the color-coded $\mathcal{P}_\infty$ in the state diagram reduced trapping strength α versus Péclet number Pe. At low trapping strengths, where thermal noise is dominant, and at high α, where the particles pack closely, the polar order is low. In between clear polar order sets in and the fluid pump develops. The pump formation criterion $\alpha \sim \sqrt{\mathrm{Pe}/N}$ with an adjusted prefactor is indicated by the lower solid line and, indeed, describes the pump formation against thermal noise. Along the dashed lines the mean density n or volume fraction of the colloids stays constant, where $n = Na^3/r_{\mathrm{hor}}^3$ and the horizon radius r_{hor} was defined below Eq. (14). For the respective densities we plot the polar order parameter versus Pe in Fig. 5 (left). Especially at higher densities the curves have a sigmoidal shape separating disordered and polar state by a relatively sharp transition. This is reminiscent to the ordering of electric or magnetic dipoles in an applied external field [52]. However, such a field does not exist here. Instead, each active particle aligns in a flow field generated by all the other microswimmers. In the following, we review shortly how we set up a mean-field theory for the self-induced order and refer to Ref. [30] for more details.

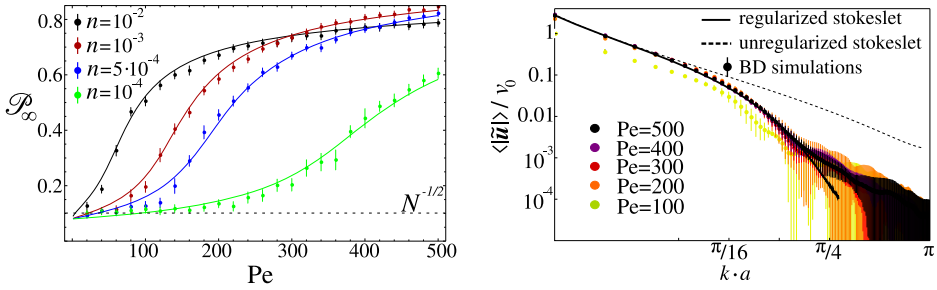

Fig. 5. (Left) Polar order parameter $\mathcal{P}_\infty$ versus activity Pe at different densities. The simulation results (dots) agree very well with the analytic result $(\mathcal{P}_\infty - N^{-1/2})/\mathcal{P}_\infty^{\max} = \mathcal{L}[3\,(\mathrm{Pe}\,\mathcal{P}_\infty/\mathrm{Pe_c})^\gamma]$ (solid lines). (Right) Directional average of the absolute value of the Fourier transform of fluid velocity, $\langle|\tilde{\boldsymbol{u}}(\boldsymbol{k})|\rangle$, plotted versus wave number k. Results from Brownian dynamics simulations (colored dots) are compared with a regularized Stokeslet (solid line) and a pure Stokeslet without regularization (dashed line). [Reprinted with permission from Ref. [30]; Copyright (2014) by the American Physical Society.]

We first determine the total flow field $\boldsymbol{u}(\boldsymbol{r})$ initiated by all the active particles by summing up all their Stokeslets from Eq. (14) and averaging over 100 uncorrelated simulation snapshots. In Fig. 5 (right) we plot the Fourier transform of $\boldsymbol{u}(\boldsymbol{r})$ averaged over all directions of wave vector $\boldsymbol{k}$ for different Péclet numbers Pe. Besides at Pe = 100, where the fluid pump has not fully developed, all other data fall on a single master curve, which we fit by a regularized Stokeslet [53],

$$\boldsymbol{u}_{\mathrm{reg}}(\boldsymbol{r}) = -\frac{v_0\epsilon}{2(r^2+\epsilon^2)^{3/2}}\left[\mathbf{1}(r^2+2\epsilon^2) + \boldsymbol{r}\otimes\boldsymbol{r}\right]\boldsymbol{e}_z\,, \tag{15}$$

also for the region inside the pump, where we use ϵ as a fit parameter. At shorter length scales clear deviations from a pure Stokeslet occur and on the scale of several particle radii, fluctuations in the particle positions lead to deviations from the regularized Stokeslet.

To formulate the mean-field theory, we start with the Smoluchowski equation (5) for the one-particle distribution function $\rho(\boldsymbol{r},\boldsymbol{e})$, where the respective translational and rotational currents are

$$\boldsymbol{J}^{\mathrm{trans}} = [v_0\boldsymbol{e} - k_{\mathrm{trap}}\boldsymbol{r}/\gamma + \boldsymbol{u}(\boldsymbol{r})]\rho \quad \text{and} \quad \boldsymbol{J}^{\mathrm{rot}} = [(\nabla\times\boldsymbol{u}(\boldsymbol{r}))/2 - D_r\mathcal{R}]\rho\,. \tag{16}$$

The particles couple to each other by the self-generated flow field $\boldsymbol{u}$, which induces advective currents both for translation and rotation. No further particle interactions are included and we neglect translational diffusion, since we are mostly interested in large Péclet numbers, Pe $\geq$ 100. The mean-field approximation now consists in taking $\boldsymbol{u}(\boldsymbol{r}) = \boldsymbol{u}_{\mathrm{reg}}(\boldsymbol{r})$ in the steady state. To proceed with an analytical treatment, we make a rough ansatz for the one-particle distribution, $\rho(\boldsymbol{r},\boldsymbol{e}) = \Phi(\boldsymbol{e})\,f(r)\,\delta(\cos(\theta) - \cos(\theta_e))\delta(\varphi-\varphi_e)$, assuming that particle orientations always point radially outward. Here θ and φ are the spherical coordinate angles of position and θ_e and φ_e those of the orientation vector $\boldsymbol{e}$ measured against the main axis of the pump along $\boldsymbol{e}_z$. This assumption holds approximately as a numerical solution of the Smoluchowski equation and Brownian dynamics simulations show [30]. Integrating the Smoluchowski equation over particle position using the ansatz for $\rho(\boldsymbol{r},\boldsymbol{e})$, we arrive at the equation for the orientational distribution function $\Phi(\boldsymbol{e})$ and its steady-state solution:

$$\partial_t\Phi(\boldsymbol{e}) = -\mathcal{R}\cdot[\langle\boldsymbol{\omega}\rangle(\boldsymbol{e}) - D_r\mathcal{R}]\Phi(\boldsymbol{e}) \qquad \longleftrightarrow \qquad \Phi(\boldsymbol{e}) = \mathrm{e}^{A\cos\theta_e}/\mathcal{N}\,. \tag{17}$$

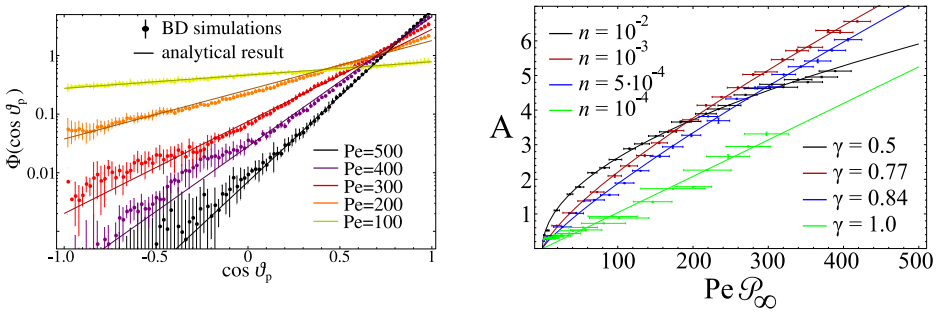

Fig. 6. (Left) Orientational distribution function for different particle activities Pe at fixed average density $n = 10^{-3}$. The simulation results (dots) are very well reproduced by $\Phi(\cos\theta_p) \sim \exp(A\cos\theta_p)$ (solid lines). (Right) Field strength A over $\mathrm{Pe}\mathcal{P}_\infty$ for different densities n. The solid lines are fits to $A \propto (\mathcal{P}_\infty \mathrm{Pe})^\gamma$. [Reprinted with permission from Ref. [30]; Copyright (2014) by the American Physical Society.]

Here, $\langle\boldsymbol{\omega}\rangle(\boldsymbol{e}) = \langle[\nabla \times \boldsymbol{u}_{\mathrm{reg}}(\boldsymbol{r})]/2\rangle = -AD_r \sin(\theta_p)\,\mathbf{e}_{\varphi_p}$ is the mean vorticity of the regularized Stokeslet and $A = \mathrm{Pe}\int_0^\infty \frac{\epsilon\, a(5\epsilon^2+2r^2)}{3(\epsilon^2+r^2)^{5/2}} r^3 f(r)\mathrm{d}r$ can be interpreted as the strength of a mean field trying to align the active particles along the z direction. Figure 6 (left) shows $\Phi(\boldsymbol{e})$ with normalization factor $\mathcal{N}$ for different Péclet numbers in very good agreement with Brownian dynamics simulations. The parameter ϵ and the radial distribution $f(r)$ necessary to determine the mean-field strength A have been extracted from fits of the flow field and the simulations, respectively.

A single swimmer orients in a mean flow field with field strength A, which is created by the swimmers themselves. This is in analogy to the molecular magnetic field in the Weiss theory for ferromagnetism. Explicitely, for the mean polar order we obtain $\mathcal{P}_\infty = \int \cos\theta_e \Phi(\boldsymbol{e})\mathrm{d}\cos\theta_e = \mathcal{L}(A) = \coth(A) - 1/A$, where $\mathcal{L}(A)$ is the Langevin function from the classical theory of magnetism [52]. In turn, the field strength A depends on the polar order parameter $\mathcal{P}_\infty$ and we find in our simulations $A \propto (\mathrm{Pe}\,\mathcal{P}_\infty)^\gamma$ with an exponent γ close to 1 for low densities and decreasing for higher densities [see Fig. 6 (right)]. This supports the formal analogy with the Weiss molecular field generalized to an exponent $\gamma \leq 1$. The Péclet number Pe takes the role of inverse temperature. The solid lines in Fig. 5 (left) are given by the implicite equation

$$(\mathcal{P}_\infty - N^{-1/2})/\mathcal{P}_\infty^{\max} = \mathcal{L}[3\,(\mathrm{Pe}\,\mathcal{P}_\infty/\mathrm{Pe_c})^\gamma]. \tag{18}$$

Due to the finite number of particles N, there is always a residual polar order $\mathcal{P}_\infty = N^{-1/2}$ and the curves are shifted accordingly. The geometric parameter $\mathcal{P}_\infty^{\max}$ considers that full alignment $\mathcal{P}_\infty = 1$ cannot be attained since the shape of the pump and the excluded volume of the particles prohibit completely parallel particle orientations. Clearly, numerical solutions of Eq. (18) with the critical Péclet number $\mathrm{Pe_c}$ and $\mathcal{P}_\infty^{\max}$ as fitting parameters fit the simulation data very well. This supports our approach introducing a mean flow field in which the active particles align.

So far, we did not include the flow fields of force dipoles typical for autonomous swimmers [54]. In Ref. [30] we find that these flow stresslets hinder alignment in agreement with previous studies on suspensions of active particles [21,23]. Neutral swimmers without the force dipoles show the strongest ordering meaning that the alignment of swimmers is mediated solely by the Stokeslets due to the harmonic trapping force. For biologically relevant systems, where the flow stresslets are small (see Ref. [21]), the reduction in the mean polar order $\mathcal{P}_\infty$ is small and the mean field theory as described above holds without further changes [30].

To conclude, the emergent collective dynamics of active Brownian particles in a harmonic trap presents an intriguing example of a non-equilibrium system, which can be mapped onto a classical equilibrium system. Specifically, the self-induced alignment of particles mediated by their own flow field is in formal agreement with spontaneous magnetization in ferromagnetic materials treated on the mean-field level.

3 Swimming in Poiseuille flow

Microswimmers often have to respond to fluid flow and confining boundaries, like sperm cells in the Fallopian tubes [55] or pathogens in blood vessels [56]. Artificial microswimmers constructed with the vision to act as drug-deliverers in the human body [57] would have to swim in narrow channels like arteries. Two properties influence the swimming in microchannels. On the one hand, vortices in flow but also pure shear flow reorient the swimming direction of microorganisms. In linear shear flow spherical microswimmers tumble due to a constant flow vorticity [58]. Vortices in Poiseuille flow in combination with bottom-heaviness due to gravitation lead to stable orientations of swimming algae cells [59]. On the other hand, microorganisms swimming near surfaces are trapped by hydrodynamic interactions [60] and ultimately escape with the help of rotational diffusion [61,62]. Finally, bacteria in Poiseuille flow show a net-upstream flux at the walls due to the interplay of confinement and flow vorticity [29,63,64] and they develop non-uniform density profiles [40,41].

All these examples show there is genuine interest in understanding generic features of microorganisms and artificial swimmers moving in Poiseuille flow. In the following, we concentrate on the deterministic motion and demonstrate the richness of possible swimming trajectories in two and three dimensions reviewing our work from Refs. [38,39]. Finally, we demonstrate how hydrodynamic interactions with channel walls modify these trajectories [38]. We treat here an ideal situation since we omit any obstacles, which a biological microswimmer encounters when moving, for example, in a blood vessel.

3.1 Basis equations

We consider a point-like microswimmer with swimming direction $\boldsymbol{e}$ and velocity v_0 moving in a Poiseuille flow through a microchannel. We assume $\mathrm{Pe} \gg 1$ to neglect thermal translational diffusion and also a large persistence number, $\mathrm{Pe}_r = \tau_r/t_f \gg 1$, where t_f is the characteristic time of the swinging and tumbling trajectories to be introduced below. Furthermore, we assume the flow strength v_f to be sufficiently large so that hydrodynamic interactions with bounding channel walls are negligible. However, we will address them in Sect. 3.4.

For an elliptical channel cross section with major axis a and b, the pressure-driven Poiseuille flow along the z direction amounts to

$$\boldsymbol{v}_P(x,y) = v_f\left[1 - \left(\frac{x}{a}\right)^2 - \left(\frac{y}{b}\right)^2\right]\boldsymbol{e}_z. \tag{19}$$

For a cylindrical channel $R_{\mathrm{ch}} = a = b$ and $b \to \infty$ means planar Poiseuille flow. The dynamics of the microswimmer is determined by vorticity vector $\boldsymbol{\Omega}_P(\boldsymbol{r})$ and strain rate tensor $\boldsymbol{E}(\boldsymbol{r})$, which for a cylindrical Poiseuille flow become

$$\boldsymbol{\Omega}_P(\boldsymbol{r}) = \nabla \times \boldsymbol{v}_P(\boldsymbol{r}) = 2v_f \frac{\rho}{R_{\mathrm{ch}}^2}\boldsymbol{e}_\phi \tag{20}$$

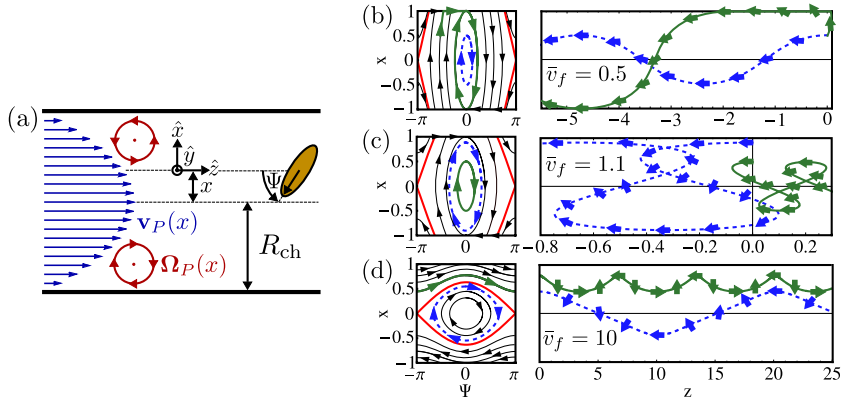

Fig. 7. (a) A microswimmer moves in the xz plane through a microchannel with channel width $2R_{\rm ch}$ under the influence of a Poiseuille flow $\boldsymbol{v}_p(x)$, which is directed along the z axis. The local vorticity $\boldsymbol{\Omega}_P(x)$ rotates the swimmer orientation, which is quantified by the angle ψ against the horizontal. (b)–(d) Phase portraits and swimming trajectories for different flow strengths $\bar{v}_f = v_f/v_0$. The microswimmer is indicated by arrows, always starts at $z = 0$, and either swings around the centerline or tumbles in one half of the channel. [Fig. (a) from Ref. [74]; courtesy of A. Zöttl. Figs. (b)–(d) reprinted with permission from Ref. [38]; Copyright (2012) by the American Physical Society.]

and

$$\boldsymbol{E}(\boldsymbol{r}) = \frac{1}{2}\left[\nabla \otimes \boldsymbol{v}_P(\boldsymbol{r}) + (\nabla \otimes \boldsymbol{v}_P(\boldsymbol{r}))^T\right] = -v_f \frac{\rho}{R_{\rm ch}^2}(\boldsymbol{e}_\rho \otimes \boldsymbol{e}_z + \boldsymbol{e}_z \otimes \boldsymbol{e}_\rho)\,. \tag{21}$$

In contrast to a passive particle, which is simply advected by the Poiseuille flow, an active particle crosses streamlines because of its self-propulsion. In addition, its swimming direction $\boldsymbol{e}$ moves on a Jeffery orbit [65], where $\boldsymbol{e}$ rotates due to the intrinsic flow vorticity $\boldsymbol{\Omega}_P$ and for non-spherical swimmer shape also due to the strain rate $\boldsymbol{E}$. Thus, for point-like active particles, meaning they are small compared to the characteristic dimensions of the flow field, the dynamics of position vector $\boldsymbol{r}(t)$ and orientation vector $\boldsymbol{e}(t)$ follow [39]

$$\frac{d}{dt}\boldsymbol{r} = v_0\boldsymbol{e} + \boldsymbol{v}_P(r) \quad \text{and} \quad \frac{d}{dt}\boldsymbol{e} = \boldsymbol{\Omega}(\boldsymbol{r},\boldsymbol{e}) \times \boldsymbol{e} \quad \text{with} \quad \boldsymbol{\Omega}(\boldsymbol{r},\boldsymbol{e}) = \frac{1}{2}\boldsymbol{\Omega}_P(\boldsymbol{r}) + G\boldsymbol{e} \times \boldsymbol{E}(\boldsymbol{r})\boldsymbol{e}. \tag{22}$$

The geometry factor $G = (\gamma^2 - 1)/(\gamma^2 + 1)$ with $G \in [0, 1)$ depends on the aspect ratio $\gamma = L/W$ of the swimmer, where L and W are its respective length and width. For spherical swimmers, where $\gamma = 1$ and $G = 0$, only the flow vorticity $\boldsymbol{\Omega}_P$ determines the swimmers angular velocity $\boldsymbol{\Omega}$.

3.2 Motion in a plane

We first concentrate on a spherical active particle swimming in the xz plane of the Poiseuille flow with the swimming direction oriented at an angle ψ against the z axis [see Fig. 7(a)] [38]. With $G = 0$ the equations of motion (22) become

$$\dot{x} = -v_0 \sin\psi \quad \text{and} \quad \dot{\psi} = \frac{v_f}{R_{\rm ch}^2}x \quad \longrightarrow \quad \ddot{\psi} + \omega^2 \sin\psi = 0 \quad \text{with} \quad \omega^2 = \frac{v_f v_0}{R_{\rm ch}^2}. \tag{23}$$

So, the orientation angle ψ obeys the same equation as the mathematical pendulum with characteristic angular frequency ω. While swimming upstream, the active particle moves on a swinging trajectory about the center line. This becomes immediately clear from Fig. 7(a). When the swimmer moves into the lower half of the channel, the vorticity of the Poiseuille flow (red circles) rotates the swimming direction $\boldsymbol{e}$ back towards the center line. The swimmer enters the upper half and again $\boldsymbol{e}$ is rotated back towards the center line and so on. We can formally introduce an Hamiltonian as a constant of motion and derive from it the equations of motion (23):

$$H = \frac{1}{2} v_f \frac{x^2}{R_{\mathrm{ch}}^2} + v_0(1 - \cos\psi) \quad \text{with} \quad \dot{x} = -\frac{\partial H}{\partial \psi} \quad \text{and} \quad \dot{\psi} = \frac{\partial H}{\partial x}, \tag{24}$$

where ψ is the generalized coordinate and $x \propto \dot{\psi}$ plays the role of the canonically conjugate momentum.

The phase portraits in Figs. 7(b)–(d) for different flow strengths $\bar{v}_f = v_f/v_0$ help to discuss the situation. The closed phase curves correspond to the swinging solutions of both the pendulum and the microswimmer as illustrated by the blue trajectory in Fig. 7(b). These solutions occur for $H < 2v_0$ since at $x = 0$ one has $|\psi| < \pi$. For small swinging amplitudes, ω from Eqs. (23) is the swinging frequency. Perfect upstream swimming along the centerline occurs at the stable fixed point at $x = \psi = 0$ of the phase portraits, where the Hamiltonian is zero. On the other hand, downstream swimming along the centerline ($\psi = \pi$ and $x = 0$) is an unstable fixed point. After a disturbance of $x = 0$, vorticity rotates the microswimmer away from the centerline, which then performs a tumbling motion as visualized by the green trajectory in Fig. 7(d). This corresponds to the circling solution of the pendulum at $H > 2v_0$. The separatrix separates both types of solutions and is defined by $H = 2v_0$, which gives $(x/R_{\mathrm{ch}})^2 = (2v_0/v_f)(1 + \cos\psi)$, [red curves in the phase portraits of Figs. 7(b)–(d)]. The separatrix fully enters the channel for flow strengths above $v_f = 4v_0$, where $|x| = 1$ at $\psi = 0$. Thus, tumbling motion can only occur for $v_f > 4v_0$.

To determine the full trajectory of the microswimmer, one has to solve $\dot{x} = -v_0 \sin\psi$ together with the dynamic equation for the z coordinate: $\dot{z} = v_f[1 - (x/R_{\mathrm{ch}})^2] - v_0 \cos\psi$. Examples are given in Figs. 7(b)–(d) for different flow strengths. If we only consider steric interactions of the swimmer with the channel wall, the swimmer crashes into the wall at $|x| = 1$ if it crosses the centerline at sufficiently large angle ψ and swimming velocity v_0 meaning $H > v_f/2$. Flow vorticity rotates the swimmer upstream until it leaves the wall at $\psi = 0$. Then it continues swimming on the swinging trajectory with $H = v_f/2$ as visualized by the green trajectory in Fig. 7(b). In summary, for $v_f < 4v_0$ the swimmer always enters a swinging motion oriented upstream, at the latest after contact with the wall, whereas it can also tumble close to the wall for $v_f > 4v_0$. While the microswimmer moves upstream for low flow strength v_f as in Fig. 7(b), with increasing v_f the Poiseuille flow can effectively drift the swimmer downstream. This happens for small v_0 in the green trajectory of Fig. 7(c) although the swimmer is always oriented upstream. As a result, the real trajectory strongly deviates from a sinusoidal oscillation. Increasing the swimming velocity v_0, net-upstream swimming is still possible as the blue trajectory in Fig. 7(c) demonstrates. Finally, Fig. 7(d) shows both swinging and tumbling trajectories, but the swimmer always drifts downstream.

Typically, microswimmers are elongated and the strain rate tensor $\boldsymbol{E}$ of the flow field also contributes to the angular frequency vector $\boldsymbol{\Omega}$ in Eqs. (22). The equations of motion now read $\dot{x} = -\sin\psi$ and $\dot{\psi} = x(v_f/R_{\mathrm{ch}}^2)(1 - G\cos 2\psi)$ [39]. We are still able to identify a constant of motion but the system cannot be formulated as a Hamiltonian dynamical system. The phase portraits of elongated swimmers again reveal swinging

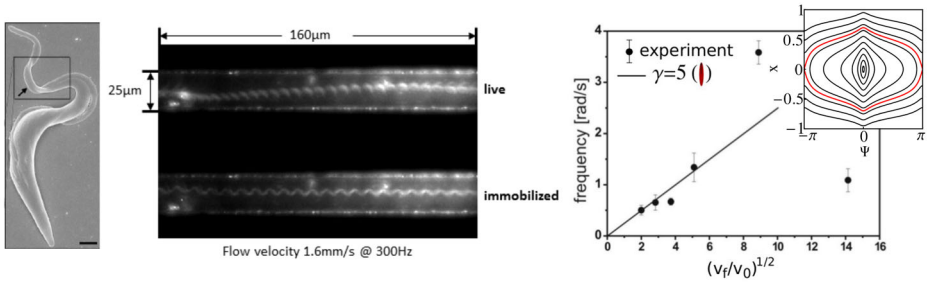

Fig. 8. (Left) Scanning electron micrograph of an African trypansome. (Middle) Stroboscopic snapshots of a trypanosome in a Poiseuille flow. Top channel: swinging trajectory of the live parasite. Bottom channel: straight trajectory of an immobilized parasite. (Right) Swinging frequency versus $v_f^{1/2}$. The solid line is a fit from theory with swimmer aspect ratio $\gamma = 5$. Inset: Phase portrait for flow strength $v_f = 5v_0$ and $\gamma = 5$, which gives a geometric factor $G = 0.92$. [(Left) Reprinted from Ref. [70] with permission from PNAS. (Middle), (Right) Reprinted from Ref. [56] with permission from Elsevier. Inset reprinted from Ref. [39] with kind permission of The European Physical Journal (EPJ).]

and tumbling solutions but their phase portraits are distorted compared to spherical swimmers. An example is given in the inset of Fig. 8 (right).

The African trypanosome is a parasite that causes the sleeping sickness [66–69]. Its cell body has the elongated shape of a spindle, to which a flagellum is attached that basically is identical to the flagellum of a sperm cell [see Fig. 8 (left)]. When a bending wave travels along the flagellum, the whole cell body is distorted while moving forward. We have recently modeled the African trypanosome and simulated its self-propulsion [71,72]. Recent experiments have shown; in a Poiseuille flow an immobilized trypanosome drifts with the streamlines whereas a live trypanosome swims upstream on a swinging trajectory as predicted by theory [56]. The series of stroboscopic snapshots of the trypanosome in Fig. 8 (middle) very nicely demonstrates the oscillatory motion in the top channel. Each snapshot reveals the bent body shape during swimming. We expect the oscillation frequency to scale with $v_f^{1/2}$. Experiments confirm this scaling for flow strengths v_f as Fig. 8 (right) shows. The solid line is a fit from theory with a reasonable aspect ratio $\gamma = 5$. The real trypansome has an aspect ratio of $\gamma \approx 8$. However, during swimming it bends and the effective aspect ratio is smaller.

3.3 Three-dimensional motion

When the orientation vector $\boldsymbol{e}$ is allowed to move out of the plane, the swimmer performs a three-dimensional motion. For planar Poiseuille flow, two constants of motion can be identified and the dynamics is thoroughly discussed in Ref. [39].

A spherical swimmer in a cylindrical channel can also be mapped on a Hamiltonian system [38]. When θ is the tilt angle of the swimming direction $\boldsymbol{e}$ out of the ρz plane, spanned by the radial and the z direction, one can formulate again a Hamiltonian and a constant of motion proportional to the angular momentum along the channel axis:

$$H = \frac{1}{2} v_f \left(\frac{\rho}{R_{\mathrm{ch}}} \right)^2 + v_0 (1 - \cos\psi \cos\theta) \quad \text{and} \quad L_z = \frac{\rho}{R_{\mathrm{ch}}} \sin\theta. \tag{25}$$

Eliminating θ by L_z, one again obtains Hamiltonian equations for the conjugate variables ψ and ρ, where ρ replaces x in Eqs. (24). Due to the non-zero angular

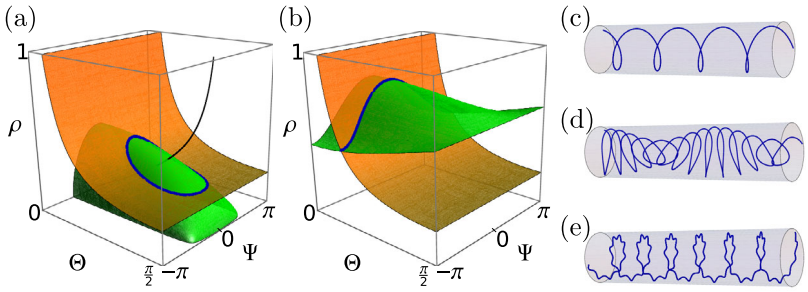

Fig. 9. (a), (b) The intersection between L_z = const. (orange) and H = const. (green) gives the swimmer trajectory in ρ-Ψ-Θ phase space. (a) Blue intersection curve: helical-like swinging trajectory for $L_z = 0.2$, $H = v_0$. Black curve: the fixed-point line leads to pure helical trajectories. (b) Blue intersection curve: helical-like tumbling trajectory for $L_z = 0.2$, $H = 3v_0$. (c–e) Sketch of trajectories in the channel representing helical motion (c), helical-like swinging (d), and tumbling motion (e). [Reprinted with permission from Ref. [38]; Copyright (2012) by the American Physical Society.]

momentum, the microswimmer performs a helical motion in the microchannel that is superimposed on the swinging and tumbling trajectories. The two constants of motion illustrated in Figs. 9(a) and (b) help to classify helical-like swinging (a) and tumbling (b) trajectories. Examples are given in Figs. 9(c)–(e).

For elongated swimmers we also find periodic trajectories in the numerical solutions of the equations of motion, although we were only able to contruct one constant of motion. Again, the trajectories are characterized by swinging and tumbling motion [39]. Finally, in channels with elliptical cross sections only one constant of motion exists leaving three independent dynamic variables out of four to describe the position of the swimmer in the channel cross section and its orientation. Therefore, the trajectories become quasiperioidic [39] and for sufficiently large flow strength even chaotic motion is observed [73].

3.4 Influence of bounding surfaces

Up to now we have neglected any hydrodynamic interactions of the microswimmer with the bounding channel walls. In the following we treat the microswimmer in the force dipole-approximation to take these hydrodynamic interactions into account [38]. They generate a wall-induced linear velocity, which has to be added to the microswimmer's velocity. Furthermore, we will neglect any wall-induced angular velocity under the assumption that the flow vorticity is much stronger. When the microswimmer approaches a wall, corrections from lubrication should be taken into account. However, for a model swimmer such as the squirmer, we know that the relevant wall-induced velocity perpendicular to the wall has the same dependence on swimmer orientation in near-field hydrodynamics as the force dipole in the far-field approximation [24], which we employ in the following.

In leading order, the flow field of a neutrally buoyant swimmer in a bulk fluid is described by a force dipole,

$$\boldsymbol{v}(\boldsymbol{r}) = \frac{p}{8\pi\eta r^2}[3(\hat{\boldsymbol{r}}\cdot\boldsymbol{e})^2 - 1]\hat{\boldsymbol{r}} \quad \text{with} \quad \hat{\boldsymbol{r}} = \boldsymbol{r}/r \tag{26}$$

and η is the viscosity of the fluid. For positive dipole strength, $p > 0$, the propelling apparatus of the swimmer is typically at the back (*pusher*), and for $p < 0$ in the front

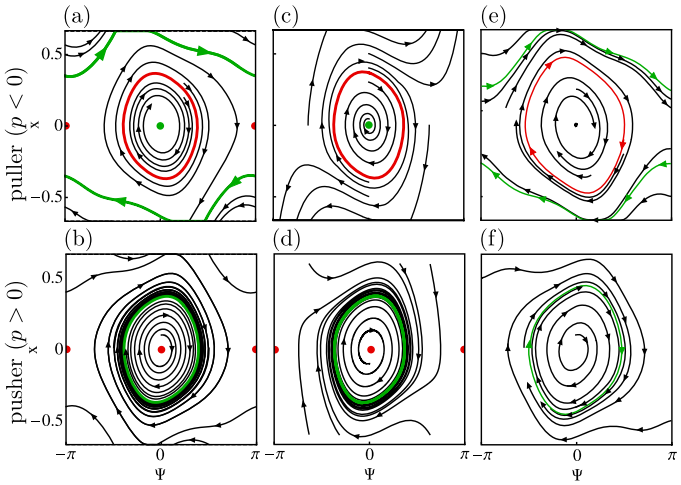

Fig. 10. Phase-space trajectories of a microswimmer in a narrow channel for $v_f/v_0 = 10$ for a puller (top) and a pusher (bottom). Green and red indicate, respectively, stable and unstable trajectories. Plots (a) and (b) are obtained by solving the equations of motion; $\dot{x} = -v_0 \sin\psi + v_w$ and $\dot{\psi} = v_f x/R_{\rm ch}^2$; (c) and (d) use the corresponding van-der-Pol system with Eq. (28); (e) and (f) are from MPCD simulations with the squirmer as a model swimmer. Each trajectory is an average over 10 individual runs. [Figs. (a), (b), (e), and (f) adapted with permission from Ref. [38]; Copyright (2012) by the American Physical Society. Figs. (c), (d) from Ref. [74]; courtesy of A. Zöttl.]

(*puller*). In Ref. [60] the authors treated force-dipole swimmers close to a plane wall taking into account image dipoles to fulfill the no-slip boundary condition at the wall. In particular, they calculated wall-induced swimmer velocities. For example, a puller swimming parallel to the wall is repelled from the wall, while a pusher is attracted and remains trapped at the wall.

In narrow channels a microswimmer permanently experiences hydrodynamic interactions with the wall. To capture the basic idea, we concentrate on planar trajectories and consider Poiseuille flow between two parallel plates located at $x/R_{\rm ch} = 1$ and $x/R_{\rm ch} = -1$. Using the results from Ref. [60], we approximate the relevant wall-induced velocity along the lateral x direction by adding up the velocities from both walls,

$$v_W = -v_0 \frac{3\bar{p}(3\sin^2\Psi - 1)}{64\pi} \left[\frac{1}{(1 - x/R_{\rm ch})^2} - \frac{1}{(1 + x/R_{\rm ch})^2} \right], \tag{27}$$

where $\bar{p} = p/(\eta v_0 R_{\rm ch}^2)$ is the reduced dipole strength. Neglecting the wall-induced angular velocity, the equations of motion become $\dot{x} = -v_0 \sin\psi + v_w$ and $\dot{\psi} = v_f x/R_{\rm ch}^2$.

Figures 10(a) and (b) show typical phase portraits generated from the equations of motion for a puller (a) and pusher (b). The swinging motion of an upstream oriented puller becomes damped and an attractive fixed point in the center exists indicated by the green dot. Repelled by both walls, meaning v_W from Eq. (27) points away from the walls at small ψ, the puller stably swims upstream along the centerline at $x = 0$. In addition, close to the walls stable tumbling states exist indicated by the green trajectories. At sufficiently strong vorticity, a swimmer tumbles with almost constant angular velocity close to a wall such that $\langle 3\sin^2\Psi - 1\rangle > 0$ and, on average, v_W from Eq. (27) is directed towards the nearest wall. This creates the stable tumbling state towards which all trajectories outside the unstable red limit cycle or separatrix converge. However, due to fluctuations of thermal or other origin the puller may cross

the separatrix and switch between stable tumbling and stable upstream swimming. A pusher behaves in the opposite way because of the opposite sign of the dipole strength. It is attracted by the wall when oriented upstream in the center of the channel, but it is pushed away from the wall when tumbling near the wall. So, all trajectories converge towards a stable limit cycle, where the pusher performs an upstream-oriented swinging motion about the centerline. The limit cycle is indicated by the green curve in Fig. 10(b).

Eliminating position $x \propto \dot{\psi}$ [see Eq. (23)] from the equations of motion, followed by an appropriate expansion in ψ, $\dot{\psi}$, we obtain the generic dynamic equation of the van-der-Pol oscillator [74]. Introducing the rescaled angle $\phi = \sqrt{3}\psi$ and rescaling time by $\omega^{-1} = R_{\mathrm{ch}}/\sqrt{v_0 v_f}$, the generic equation reads

$$\ddot{\phi} - \epsilon(1-\phi^2)\dot{\phi} + \phi = 0 \quad \text{with} \quad \epsilon = 3\bar{p}/[16\pi(v_f/v_0)^{1/2}]. \tag{28}$$

The phase portrait of the pusher ($\epsilon \propto p > 0$) in Fig. 10(d) reproduces the results from the complete theory (b), while for the puller ($\epsilon \propto p < 0$) in Fig. 10(c) the stable tumbling motion is missing due to the approximations. Finally, we also performed full hydrodynamic simulations with the squirmer as a model swimmer using the simulation method of multi-particle collision dynamics (MPCD). The resulting phase portraits in Fig. 10(e),(f) agree with the analytic theory.

Disregarding hydrodynamic interactions with bounding channel walls, a microswimmer in Poiseuille flow behaves like a conservative dynamical system. In some cases, we can even map it on a Hamiltonian system. Hydrodynamic interactions change the qualitative behavior to a dissipative dynamical system, where fixed points and limit cycles, either stable or unstable, exist. We completely neglected here any stochastic motion. To treat it, one has to study the Smoluchowski equation for the propability distribution function $\rho(\boldsymbol{r}, \boldsymbol{e}, t)$. However, the features discussed here for the deterministic trajectories will certainly determine the full problem.

4 Conclusions

Understanding the nonequilibrium of active particles is one of the challenging questions in statistical physics today. We gave here some examples how microswimmers behave under external fields. Active Brownian particles sediment like passive particles but with a sedimentation length that increases quadratically in the swimmer Peclet number. This is due to a larger effective diffusivity and polar order that develops along the vertical. Bottom-heavy swimmers with sufficiently large swimming speed can invert the sedimentation profile.

Active Brownian particles in a three-dimensional harmonic trap and interacting by their flow fields form polar order by spontaneous symmetry breaking and thereby pump fluid. A mean-field theory in analogy to the Weiss theory of ferromagnetism, which uses as a mean flow field a regularized stokeslet generated by all microswimmers, reproduces the results from particle-based Brownian dynamics simulations.

Finally, a swimmer under Poiseuille flow behaves like a conservative dynamical system and moves on swinging and tumbling trajectories. Swinging around the channel centerline has been observed in experiments with the African trypanosome. Hydrodynamic interactions with bounding surfaces introduce "dissipation". For pushers they stabilize straight swimming against the flow and tumbling close to the channel wall, while pushers always move on a swinging trajectory with a specific amplitude as limit cycle.

The work reviewed in this article was done together with M. Enculescu, M. Hennes, K. Wolff, A. Zöttl. Support from the Deutsche Forschungsgemeinschaft (DFG) within the priority program SPP 1726 "Microswimmers – from Single Particle Motion to Collective Behaviour" (STA 352/11) is gratefully acknowledged.

References

1. M.E. Cates, Rep. Prog. Phys. **75**, 042601 (2012)
2. P. Romanczuk, M. Bär, W. Ebeling, B. Lindner, L. Schimansky-Geier, Eur. Phys. J. Special Topics **202**, 1 (2012)
3. M.C. Marchetti, J.-F. Joanny, S. Ramaswamy, T.B. Liverpool, J. Prost, M. Rao, R.S. Simha, Rev. Mod. Phys. **85**, 1143 (2013)
4. H.H. Wensink, J. Dunkel, S. Heidenreich, K. Drescher, R.E. Goldsteinc, H. Löwen, J.M. Yeomans, Proc. Natl. Acad. Sci. USA **109**, 14308 (2012)
5. I. Theurkauff, C. Cottin-Bizonne, J. Palacci, C. Ybert, L. Bocquet, Phys. Rev. Lett. **108**, 268303 (2012)
6. J. Palacci, S. Sacanna, A.P. Steinberg, D.J. Pine, P.M. Chaikin, Science **339**, 936 (2013)
7. O. Pohl, H. Stark, Phys. Rev. Lett. **112**, 238303 (2014)
8. J. Tailleur, M.E. Cates, Phys. Rev. Lett. **100**, 218103 (2008)
9. Y. Fily, M.C. Marchetti, Phys. Rev. Lett. **108**, 235702 (2012)
10. G.S. Redner, M.F. Hagan, A. Baskaran, Phys. Rev. Lett. **110**, 055701 (2013)
11. I. Buttinoni, J. Bialké, F. Kmmel, H. Lwen, C. Bechinger, T. Speck, Phys. Rev. Lett. **110**, 238301 (2013)
12. J. Stenhammar, A. Tiribocchi, R.J. Allen, D. Marenduzzo, M.E. Cates, Phys. Rev. Lett. **111**, 145702 (2013)
13. T. Speck, J. Bialké, A.M. Menzel, H. Löwen, Phys. Rev. Lett. **112**, 218304 (2014)
14. T. Speck, Eur. Phys. J. Special Topics **225**, 2287 (2016)
15. T.J. Pedley, J.O. Kessler, Annu. Rev. Fluid Mech. **24**, 313 (1992)
16. A. Ordemann, G. Balazsi, F. Moss, Physica A **325**, 260 (2003)
17. R.A. Simha, S. Ramaswamy, Phys. Rev. Lett. **89**, 058101 (2002)
18. T. Ishikawa, T.J. Pedley, Phys. Rev. Lett. **100**, 088103 (2008)
19. D. Saintillan, M.J. Shelley, Phys. Rev. Lett. **100**, 178103 (2008)
20. A. Baskaran, M.C. Marchetti, Proc. Natl. Acad. Sci. USA **106**, 15567 (2009)
21. A.A. Evans, T. Ishikawa, T. Yamaguchi, E. Lauga, Phys. Fluids **23**, 111702 (2011)
22. J.J. Molina, Y. Nakayama, R. Yamamoto, Soft Matter **9**, 4923 (2013)
23. F. Alarcón, I. Pagonabarraga, J. Mol. Liq. **85**, 56 (2013)
24. A. Zöttl, H. Stark, Phys. Rev. Lett. **112**, 118101 (2014)
25. J. Palacci, C. Cottin-Bizonne, C. Ybert, L. Bocquet, Phys. Rev. Lett. **105**, 088304 (2010)
26. M. Enculescu, H. Stark, Phys. Rev. Lett. **107**, 058301 (2011)
27. K. Wolff, A.M. Hahn, H. Stark, Eur. Phys. J. E **36**, 43 (2013)
28. W.M. Durham, J.O. Kessler, R. Stocker, Science **323**, 1067 (2009)
29. R.W. Nash, R. Adhikari, J. Tailleur, M.E. Cates, Phys. Rev. Lett. **104**, 258101 (2010)
30. M. Hennes, K. Wolff, H. Stark, Phys. Rev. Lett. **112**, 238104 (2014)
31. Y. Hatwalne, S. Ramaswamy, M. Rao, R.A. Simha, Phys. Rev. Lett. **92**, 118101 (2004)
32. A. Sokolov, I.S. Aranson, Phys. Rev. Lett. **103**, 148101 (2009)
33. S. Rafai, L. Jibuti, P. Peyla, Phys. Rev. Lett. **104**, 098102 (2010)
34. H. López, J. Gachelin, C. Douarche, H. Auradou, E. Clément, Phys. Rev. Lett. **115**, 028301 (2015)
35. E. Clement, A. Lindner, C. Douarche, H. Auradou, Eur. Phys. J. Special Topics **225**, 3089 (2016)
36. C. Torney, Z. Neufeld, Phys. Rev. Lett. **99**, 078101 (2007)
37. N. Khurana, J. Blawzdziewicz, N.T. Ouellette, Phys. Rev. Lett. **106**, 198104 (2011)
38. A. Zöttl, H. Stark, Phys. Rev. Lett. **108**, 218104 (2012)
39. A. Zöttl, H. Stark, Eur. Phys. J. E **36**, 4 (2013)
40. R. Rusconi, J.S. Guasto, R. Stocker, Nature Phys. **10**, 212 (2014)

41. R. Rusconi, R. Stocker, Curr. Opin. Microbiol. **25**, 1 (2015)
42. J.R. Howse, R.A.L. Jones, A.J. Ryan, T. Gough, R. Vafabakhsh, R. Golestanian, Phys. Rev. Lett. **99**, 048102 (2007)
43. R. Golestanian, Phys. Rev. Lett. **108**, 038303 (2012)
44. K. Drescher, K.C. Leptos, I. Tuval, T. Ishikawa, T.J. Pedley, R.E. Goldstein, Phys. Rev. Lett. **102**, 168101 (2009)
45. F. Ebert, P. Dillmann, G. Maret, P. Keim, Rev. Sci. Instrum. **80**, 083902 (2009)
46. J. Yan, M. Bloom, S.C. Bae, E. Luijten, S. Granick, Nature **491**, 578 (2012)
47. C.R. Williams, M.A. Bees, J. Exp. Biol. **214**, 2398 (2011)
48. S. Childress, M. Levandowsky, E.A. Spiegel, J. Fluid Mech. **69**, 591 (1975)
49. T.J. Pedley, J.O. Kessler, J. Fluid Mech. **212**, 155 (1990)
50. M.A. Bees, N.A. Hill, Phys. Fluids **10**, 1864 (1998)
51. M. Hennes, *Strukturbildung aktiver Teilchen mit hydrodynamischer Wechselwirkung*, master thesis, Technische Universität Berlin (2013)
52. N.W. Ashcroft, N.D. Mermin, *Solid State Physics* (Harcourt, Orlando, 1976)
53. R. Cortez, L. Fauci, A. Medovikov, Phys. Fluids **17**, 031504 (2005)
54. E. Lauga, T.R. Powers, Rep. Prog. Phys. **72**, 096601 (2009)
55. J.A. Riffell, R.K. Zimmer, J. Exp. Biol. **210**, 3644 (2007)
56. S. Uppaluri, N. Heddergott, E. Stellamanns, S. Herminghaus, A. Zöttl, H. Stark, M. Engstler, T. Pfohl, Biophys. J. **103**, 1162 (2012)
57. B.J. Nelson, I.K. Kaliakatsos, J.J. Abbott, Annu. Rev. Biomed. Eng. **12**, 55 (2010)
58. B. ten Hagen, R. Wittkowski, H. Löwen, Phys. Rev. E **84**, 031105 (2011)
59. J.O. Kessler, Nature (London) **313**, 218 (1985)
60. A.P. Berke, L. Turner, H.C. Berg, E. Lauga, Phys. Rev. Lett. **101**, 038102 (2008)
61. K. Drescher, J. Dunkel, L.H. Cisneros, S. Ganguly, R.E. Goldstein, Proc. Natl. Acad. Sci. USA **108**, 10940 (2011)
62. K. Schaar, A. Zöttl, H. Stark, Phys. Rev. Lett. **115**, 038101 (2015)
63. J. Hill, O. Kalkanci, J.L. McMurry, H. Koser, Phys. Rev. Lett. **98**, 068101 (2007)
64. A. Costanzo, R. Di Leonardo, G. Ruocco, L. Angelani, J. Phys.: Condens. Matter **24**, 065101 (2012)
65. G.B. Jeffery, Proc. R. Soc. London Ser. A **102**, 161 (1922)
66. K.S. Ralston, Z.P. Kabututu, J.H. Melehani, M. Oberholzer, K.L. Hill, Annu. Rev. Microbiol. **63**, 335 (2009)
67. M. Engstler, T. Pfohl, S. Herminghaus, M. Boshart, G. Wiegertjes, N. Heddergott, P. Overath, Cell **131**, 505 (2007)
68. N. Heddergott, T. Krüger, S.B. Babu, A. Weia, E. Stellamans, S. Uppaluri, T. Pfohl, H. Stark, M. Engstler, PLoS Pathogen **8**, e1003023 (2012)
69. T. Krüger, M. Engstler, Eur. Phys. J. Special Topics **225**, 2157 (2016)
70. J.A. Rodríguez, M.A. Lopez, M.C. Thayer, Y. Zhao, M. Oberholzer, D.D. Chang, N.K. Kisalu, M.L. Penichet, G. Helguera, R. Bruinsma, K.L. Hill, J. Miao, Proc. Natl. Acad. Sci. USA **106**, 19322 (2009)
71. S.B. Babu, H. Stark, New J. Phys. **14**, 085012 (2012)
72. D. Alizadehrad, T. Krüger, M. Engstler, H. Stark, PLoS Comput. Biol. **11**, e1003967 (2015)
73. A. Zöttl, I. Dudas, H. Stark, in preparation
74. A. Zöttl, *Hydrodynamics of Microswimmers in Confinement and in Poiseuille Flow*, Ph.D. thesis, Technische Universität Berlin (2014)